Monthly Notices of the ROYAL ASTRONOMICAL SOCIETY

MNRAS **551**, 1–17 (2026)
Advance Access publication 2026 July 28
https://doi.org/10.1093/mnras/stag1428

A survey for variable young stars with small telescopes – XI. Spot lifetimes and coverage distributions

Dirk Froebrich ,[1★] Carys Herbert ,[1,2] Aleks Scholz,[3] Benjamin W. Ryan ,[1] Siegfried Vanaverbeke ,[4,5,6] Jochen Eislöffel ,[7] Cledison Marcos da Silva,[8,9] Michel Michaud,[10] Kathy Griffiths,[8,11,12,13] Ari M. Siqueira,[8,9,11] Thomas Urtly,[11] Francisco C. Soldán Alfaro,[8,14,15] George Fleming,[11] Gregg L. Ruppel,[16] Domenico Licchelli,[17,18] Stephen R. L. Futcher,[8,11,19,20] Ivan L. Walton,[11] Matthias Kolb,[21,22] Mario Morales Aimar,[14,23] Geoffrey Stone ,[8,24] Yenal Öğmen,[25] Simon Francis Dawes,[11,26] Franz-Josef Hambsch ,[5,8,21,27] Nick J. Quinn,[11] Juan-Luis González-Carballo,[8,14,28] Franky Dubois,[4,5] José Luis Salto González,[14,29,30] Adam Popowicz ,[31] Krzysztof Bernacki ,[31] Slawomir Bednarz ,[31] Tim Nelson,[19,32] Tony Vale,[8,11,12,33] Tonny Vanmunster,[34,35] Georg Piehler,[36] Stephen C. Percy,[37] Jordi Berenguer Amatller,[14] Jacopo Fallai,[38] Amritanshu Vajpayee ,[39,40] Faustino García de la Cuesta,[41] Rafael Castillo García,[14,42] Dawid Moździerski,[43] Krzysztof Kotysz,[43,44] Przemysław J. Mikołajczyk ,[43,45] Holly Stokes-Geddes,[1] Matthew D. Dickers ,[1] Ivana I. Grozdanova,[1] Chiara F. Kawohl,[1] Aashini L. Patel ,[1] James S. Urquhart [1] and Tim M. Kinnear[1]

Affiliations are listed at the end of the paper

Accepted 2026 July 24. Received 2026 July 20; in original form 2026 May 22

ABSTRACT

We present a homogeneous analysis of rotational variability and spot properties in young stellar objects (YSOs) across multiple star-forming regions observed by the HOYS (Hunting Outbursting Young Stars) project. From over 2000 candidate members, we identify 144 YSOs with robust periodic signals and well-constrained multiband amplitudes. The sample has a median age of ~1 Myr, effective temperatures of 3500–6500 K (masses ~0.6–2 $M_\odot$), and is dominated by Class 2 objects, one third of which exhibit inner disc dust emission. The rotation period distribution is strongly bimodal, with 55 per cent fast rotators ($P < 5.5$ d) and 45 per cent slow rotators. Fast rotators are predominantly inner disc-less, whereas slow rotators include both disc-bearing and disc-free systems, indicating that disc braking alone cannot explain the observed rotational states. We derive spot properties from multiband amplitudes and find that, after correcting for observational biases, the intrinsic cold-spot coverage distribution of fast rotators is well described by an exponential function. This implies that small spot coverages are intrinsically much more common than large ones, consistent with stochastic magnetic flux emergence governing spot formation. In contrast, slow rotators show a pronounced deficit of small cold spots. After considering observational biases and alternative physical explanations, we conclude that small spots on slowly rotating YSOs have significantly shorter lifetimes. These results provide new evidence that magnetic surface structure and its evolution depend on stellar rotation, placing new empirical constraints on models of magnetic activity and angular momentum evolution in young stars.

Key words: stars: formation – stars: pre-main-sequence – stars: rotation – starspots – stars: variables: T Tauri, Herbig Ae/Be.

1 INTRODUCTION

Stellar rotation is a key parameter in early stellar evolution, governing angular momentum redistribution, magnetic activity, and star–disc interactions. Observations of young stellar objects (YSOs) show a wide dispersion in rotation periods and associated variability, indicating complex regulation mechanisms. Variability on time-scales of days is typically linked to structures within the corotation radius or on the stellar surface (A. M. Cody et al. 2014; D. Froebrich et al. 2021; C. Herbert, D. Froebrich & A. Scholz 2023), while longer-term variability can arise from oc-

★ E-mail: df@kent.ac.uk

cultations by circumstellar material on time-scales from days to years (e.g. J. F. Lightfoot 1989; W. J. Fischer et al. 2023), or changes in long-term accretion rates (e.g. M. Audard et al. 2014). The rotation of a young star is initially inherited from its parent molecular cloud, yet by the main sequence its angular momentum is reduced by ∼6–7 orders of magnitude (A. Belloche 2013). During the first few Myr, rotation rates remain approximately constant despite ongoing accretion, implying efficient angular momentum loss, after which stars spin-up as they contract towards the zero-age main sequence, reaching periods as short as ∼0.2–0.3 d, before spinning down again due to magnetized winds (B. Reipurth, D. Jewitt & K. Keil 2007; J. Bouvier et al. 2014). Thus, the observed period distribution of YSOs is bimodal (e.g. W. Herbst et al. 2002, 2007; M. V. Rodríguez-Ledesma, R. Mundt & J. Eislöffel 2009, 2010; X.-L. Wang et al. 2023), indicating two distinct rotational states and suggesting that the transition between them occurs on relatively short time-scales.

A widely adopted explanation for this behaviour is disc braking, in which magnetic coupling between the star and its protoplanetary disc regulates stellar rotation by extracting angular momentum. This can be achieved in various ways, e.g. by disc locking (A. Koenigl 1991), or accretion-powered winds (S. Matt & R. E. Pudritz 2005). Observational evidence supports a link between slow rotation and accretion, particularly for stars in the mass range 0.4–1.2 $M_{\odot}$ (C. Fallscheer & W. Herbst 2006), and suggests that the magnetically coupled region is confined to the vicinity of the corotation radius (C. Zanni & J. Ferreira 2013). However, the efficiency of this mechanism and its ability to reproduce observed rotation distributions remain uncertain. The development of a radiative core on time-scales of 0.5–10 Myr can alter the stellar magnetic field topology, weakening the large-scale dipolar component required for effective disc braking (F. Gallet, C. Zanni & L. Amard 2019). Moreover, some studies find no statistically significant correlation between accretion indicators and rotation period (A. Sicilia-Aguilar et al. 2006), and the coexistence of fast rotators with discs and slow rotators without discs indicates that additional processes, such as magnetic field evolution, binarity, or rapid disc dispersal, must play an important role. Together, these results suggest that while disc braking provides a useful framework, it does not fully account for the diversity of rotational properties observed in YSOs.

Cold surface spots on YSOs are the manifestation of strong stellar magnetic fields that inhibit convection, analogous to sunspots but on a much larger scale. Solar observations provide a useful reference framework: sunspots trace a cyclic magnetic field with well-defined polarity patterns (G. E. Hale et al. 1919), although a small fraction deviate from this behaviour (J. Li 2018). In YSOs, magnetic field strengths reach a few kilogauss (C. M. Johns-Krull 2007), significantly exceeding solar values (H. W. Babcock 1961), leading to larger, more stable spots that can cover tens of per cent of the stellar surface. These spots exhibit temperature contrasts of several hundred to ∼1400 K below the photosphere (K. N. Grankin et al. 2008) and their overall coverage decreases with stellar age (B. M. Morris 2020). Photometric monitoring demonstrates that spot modulation is a dominant source of variability, and most YSOs show signatures consistent with cold spot coverage (J. Bouvier et al. 1999; J. M. Carpenter, L. A. Hillenbrand & M. F. Skrutskie 2001).

Hot spots arise from magnetospheric accretion, where disc material is channelled along magnetic field lines onto the stellar surface, producing localized heating and variability. These spots drive a range of observed light-curve morphologies, from burst-like behaviour linked to episodic accretion (J. Stauffer et al. 2016; A. M. Cody et al. 2017) to stochastic variability caused by unstable accretion flows (J. Stauffer et al. 2016), and quasi-periodic modulation reflecting rotation combined with evolving accretion structures (A. M. Cody et al. 2014). Contrary to the classical picture of small, very hot accretion shocks, observations reveal a wide diversity in spot properties: temperature contrasts can be only a few hundred Kelvin above the photosphere with large filling factors up to ∼40 per cent (e.g. A. Scholz et al. 2012; I. Bozhinova, A. Scholz & J. Eislöffel 2016; A. Sicilia-Aguilar et al. 2023). In other cases, hot spots occupy less than 1 per cent of the surface (L. Ingleby et al. 2013). Extended, low-density accretion structures can also dominate optical emission (C. C. Espaillat et al. 2021), highlighting the complexity of accretion-driven variability in YSOs.

The Hunting Outbursting Young Stars (HOYS) citizen science project combines long-term monitoring (from multiyear to decade long) with multiband optical photometry in standard filters, from a coordinated network of amateur and professional observers that enables high-cadence homogeneous coverage across multiple regions (D. Froebrich et al. 2018; J. J. Evitts et al. 2020). Thus, it provides a uniquely suited data set for investigating the evolution of rotational variability in YSOs. Previous HOYS studies have demonstrated its capability to characterize rotational variability and surface features in detail. For example, individual objects such as V1598 Cyg exhibit rapid rotation and spot-driven variability (D. Froebrich et al. 2020), while systematic analyses in IC 5070 revealed a clearly bimodal period distribution and allowed the derivation of spot temperatures and surface coverage for sizeable samples of YSOs (D. Froebrich et al. 2021; C. Herbert et al. 2023, 2024). These works show that most variability is dominated by cold spots with large filling factors, along with a smaller population of warm or hot spots linked to accretion, but are limited to individual regions and relatively modest sample sizes.

The primary motivation of this study is to extend this analysis across multiple star-forming regions within the HOYS data set, thereby testing whether key observational features, such as bimodal period distributions, spot properties, and the connection between rotation and circumstellar discs, are universal or environment-dependent. Expanding the sample enables a statistically robust characterization of rotational and spot properties, while consistent period analysis across epochs provides constraints on spot lifetimes and on the intrinsic distribution of spot properties. By linking rotation periods, variability amplitudes, and disc indicators, this work aims to assess the role of magnetic star–disc interaction in regulating angular momentum and to disentangle the relative contributions of magnetic activity, accretion, and circumstellar material in shaping YSO variability.

This paper is structured as follows. In Section 2, we detail the extraction and calibration of our HOYS data, the period and effective temperature determination, and the spot property calculations. The period distribution and the YSO properties are discussed in Section 3. In Section 4, we discuss how our results compare to previous work, and what the implications of the spot property distributions are for the nature of the cold and warm spots on YSOs.

Table 1. HOYS target regions investigated for periodic YSOs. We list the region name, the three-digit region ID, the nominal centre coordinates for the fields, the number of light curves N_{LC} and slices N_{SL} investigated with sufficient data, and the number of light curves and slices found to show a periodic signal.

Region		RA/Dec. (J2000)		Sufficient data		Periodic	
Name	ID	h:m:s	°:′:″	N_{LC}	N_{SL}	N_{LC}	N_{SL}
NGC 1333	001	03:29:02	+31:20:54	20	–	–	–
IC 348	002	03:44:34	+32:09:48	79	–	–	–
M42	003	05:35:17	−05:23:28	74	155	9	34
NGC 2264	004	06:40:58	+09:53:42	285	1	–	–
σ Ori	005	05:38:45	−02:36:00	69	324	17	90
λ Ori	006	05:35:06	+09:56:00	18	–	–	–
L1641 N	007	05:36:19	−06:22:12	108	130	11	22
NGC 2244	008	06:31:55	+04:56:30	58	–	–	–
Berkeley 86	110	20:20:12	+38:41:24	229	25	–	–
P Cyg	111	20:17:47	+38:01:59	196	15	–	–
IC 1396 N	114	21:40:42	+58:16:06	150	405	17	71
IC 1396 A	115	21:36:35	+57:30:36	187	528	25	78
NGC 7129	116	21:42:56	+66:06:12	25	24	1	4
IC 5070	118	20:51:00	+44:22:00	136	970	31	211
IC 5146	119	21:53:29	+47:16:01	65	121	9	19
V898 Ori	202	05:40:26	−07:05:37	13	30	3	8
YY Ori	203	05:34:48	−05:57:57	52	160	9	32
V555 Ori	210	05:35:09	−04:46:52	80	226	10	48
Gaia 19 fct	213	07:09:21	−10:29:35	145	409	2	3
Gaia 19 eyy	214	08:30:42	−41:33:43	58	229	–	–

2 DATA AND METHODOLOGY

In this section, we provide a brief overview of the data and methodology used. They are mostly identical to what has been done in our previous work in IC 5070 (D. Froebrich et al. 2021; C. Herbert et al. 2023, 2024), but they are applied here to all HOYS fields. Any differences are detailed in the following.

2.1 Data, calibration, and object selection

All photometry data used are from the HOYS citizen science project (D. Froebrich et al. 2018), which monitors 25 young (age less than 10 Myr) and nearby (distance less than 1 kpc) star clusters and star-forming regions with a combination of amateur, university, and professional telescopes. The aim of the project is to obtain daily images in optical broad-band filters over about 25 yr. The images are calibrated relative to a set of reference images taken under photometric conditions in the V, R_C, and I_C filters. These will be referred to as V, R, and I, throughout, for simplicity. Data in other filters (U, B, and Hα) are available but not used in this work. All data are colour-corrected (in case of non-ideal observing conditions or non-standard filters) following the procedures established in J. J. Evitts et al. (2020).

In D. Froebrich et al. (2024), we used *Gaia* Data Release 3 (DR3) data (Gaia Collaboration 2016, 2023) to generate a full list of cluster members in all HOYS target regions based on their astrometric properties (parallax and proper motion). These objects therefore have distances and space motions consistent with membership of the respective young star-forming regions, making contamination by unrelated foreground or background stars, including evolved giants, very small. In that work, a total of just over 3000 objects were selected as potential HOYS cluster members for investigation. Their light curves were extracted from our data base on 2022 October 21 and calibrated using the procedures detailed above. Light curves with at least 100 data points in each of the three filters are available for 2047 of these. Only those are investigated in this work.

For all potential cluster members, we used *Gaia* DR3 (Gaia Collaboration 2016, 2023) cross-matches to the Two Micron All-Sky Survey (2MASS; M. F. Skrutskie et al. 2006) and the *Wide-Field Infrared Survey Explorer* (*WISE*) All-Sky Catalogue (R. M. Cutri et al. 2013) to obtain their near-infrared (J, H, and K) and mid-infrared ($W1$, $W2$, $W3$, and $W4$) magnitudes and colours. In some cases, the objects did not have any K-band data available in 2MASS. For these, we extracted data from the UKIRT Infrared Deep Sky Survey (UKIDSS; A. Lawrence et al. 2007), in particular from the Galactic Plane Survey (GPS; P. W. Lucas et al. 2008).

A note on notation: throughout the paper, we are investigating the light curves, or parts of them, for our objects in multiple filters (V, R, and I). In some cases, we will only need to refer to data in an individual filter, and in others to the entire set of data in all filters. Thus, for simplicity and to maintain the notation used in C. Herbert et al. (2024), we will denote these data sets using {} around the symbol for the shortest wavelength filter included in the set. For example, $\{V\}$ refers to the data set in the filters V, R, and I.

2.2 Light-curve slicing

We plan to investigate the spot properties on the observed YSOs over time. For this purpose, all light curves have been dissected (sliced) into blocks of 6 months' length. This has been done with an oversampling of two. In other words, a 6-month-long slice is created every 3 months for all light curves. This follows the procedure developed for the field IC 5070 in C. Herbert et al. (2024). The earliest data point in any of our light curves is from 2013. For each object, the starting date for the first slice is therefore set on the date of its worst observability in the Northern hemisphere in 2013. This is the date when it has the lowest altitude at midnight.

For all objects, only slices that contained at least 50 data points in each of $\{V\}$ were retained. The majority of light curves did not have the necessary observational cadence to meet this threshold for their entirety. From the 2047 light curves, 918 objects had at least one slice with sufficient data. In total, there are 3752 individual, 6-month-long slices. Table 1 lists the HOYS target regions (including their number and nominal coordinates) with investigated light curves, their number, and the number of slices with sufficient data. Unlisted HOYS regions do not have any light curves with sufficient data.

2.3 Period search and amplitude determination

The search for periodic variability has been conducted following our investigations in D. Froebrich et al. (2021). In this work, we established that the most efficient way of searching for periodic signals in inhomogeneously sampled light curves such as those from HOYS is a combination of different methods. In particular, we combine the results of the L1Boot, L1Beta, L2Beta, and generalized Lomb–Scargle (GLS) periodogram methods. The details of these are discussed in the appendix of D. Froebrich et al. (2021). We follow the procedures for period determination in each slice and object, as outlined in C. Herbert et al. (2024) for the IC 5070 region, with some minor adjustments.

For each object, only slices with 50 data points in all $\{V\}$ filters were considered, since the amplitudes in all three filters are required to determine the spot properties later on. Periodograms with 1000 test periods, homogeneously sampled in frequency between 1/0.5 and 1/20 d^{-1} are determined for each filter, periodogram method, and slice. Candidate periods for a slice were accepted if the maximum periodogram power exceeded 0.15 (for L1Boot, L1Beta, and L2Beta) or the lowest FAP (false alarm probability) was below 0.1 per cent (for GLS). Each of these candidate periods must be within 5 per cent of each other in at least two of the three filters by the same method. All candidate periods within 1 per cent of 0.5, 1, or 20 d were removed, as they are either at the edges of the investigated parameter space or too close to the typical observing cadence. This generates a list of candidate periods for each object.

These lists can contain different periods. In principle, for a given object, we can have four candidate periods per slice, one from each of the methods. Thus, we clustered the list of all candidate periods per object to identify groups. If the most populous group contained more than 2/3rd of all candidate periods (and there are at least five in the group), the median of all periods in that group was chosen as the candidate period for the object. If for an object none of the groups had sufficient data, the phase-folded light curves were inspected manually, and visually good-quality periods were added. The minimum number of candidate periods accepted was two, which were detected by two different methods in a single slice.

Finally, for each object with a candidate period, the final period was determined as follows. A simple Lomb–Scargle periodogram is applied over the entire light curve in each filter, centred on the median of the candidate periods in the primary group. We used 1000 homogeneously distributed test periods within 10 per cent of that median. The period associated with the highest peak in the periodogram was determined in each filter. The median of these is taken as the final period for the object, and the standard deviation as the uncertainty. The full list of all identified periodic sources is shown in Table A1 in Appendix A. In that table, we list the *Gaia* DR3 ID, the right ascension and declination, as well as the measured period and the uncertainty.

All slices of the periodic variables with sufficient data were phase folded with the respective final period for each object. The observed sets of peak-to-peak amplitudes $\left(\hat{A}^{o}_{\{V\}}\right)$ were calculated following C. Herbert et al. (2024). These were taken from the running median in the light-curve phase plot, smoothed over 0.1 in phase. The associated uncertainties are the standard deviation of the phase-folded light curve from the smoothed running median. In addition, the phase position of the minima and maxima of the smoothed running median was recorded. Only slices where the signal-to-noise ratio for the peak-to-peak amplitudes in all three filters was greater than 3 and where minima and maxima in the phase plots aligned within 0.125 are considered for spot fitting. All phase-folded light curves were inspected, and five additional slices were removed because the running median did not represent the data well. This is generally due to gaps in the data in phase space, which commonly occur with periods close to integer days. In total, 620 sets of amplitudes $\hat{A}^{o}_{\{V\}}$ in 144 YSOs were identified as reliable. Table 1 lists their numbers for each of the HOYS regions.

2.4 Effective temperature estimates and spot fitting

The fitting of spot properties on the YSOs follows the procedure outlined in C. Herbert et al. (2023). This only requires knowledge of the effective temperature $T_{\rm eff}$ of the star and the sets of amplitudes from the spot-induced periodic variability. In our previous analyses of spot properties (C. Herbert et al. 2023, 2024), we focused on the YSOs in the IC 5070 region. There, almost all objects had effective temperatures available from M. Fang et al. (2020). For sources without, we used the best estimates based on their position in the *Gaia* colour–magnitude diagram. Unfortunately, this is not an option for most other HOYS regions. There are no consistent catalogues of effective temperatures for all YSOs in these fields available. As demonstrated in C. Herbert et al. (2023), systematic changes of up to ± 400 K in the adopted $T_{\rm eff}$ values do not alter the inferred spot property distributions beyond the statistical uncertainties. Thus, we outline below our new method to obtain approximate effective temperatures from survey broadband colours for all HOYS YSOs.

We extracted all *Gaia* members in the North American and Pelican Nebula (NAP) region that have an effective temperature listed in M. Fang et al. (2020). This list was limited to $T_{\rm eff} < 8000$ K. In addition, we extracted all *Gaia* DR3 magnitudes (G, BP, RP) and parallax values. The G-band magnitude was converted into an absolute magnitude G_G using the parallax, without considering any extinction. In addition, all 2MASS and *WISE* magnitudes (if available) were obtained. Homogeneous and reliable extinction estimates are not available for the full calibration sample. This leaves a list of $\sim$200 members of the NAP cluster with effective temperatures in M. Fang et al. (2020).

In order to fit the effective temperature in this sample based on their absolute G-band magnitude and different colours, we define the function shown in equation (1). There, the symbols take their usual meaning, and the p_i are free parameters. The two additional colours C_1 and C_2 represent any colour that can be created from the magnitudes of *Gaia* (G, BP, RP), 2MASS/UKIDSS GPS (J, H, K), and *WISE* ($W1$, $W2$). We do not consider $W3$ or $W4$ because these are not available at a high signal-to-noise ratio for most objects:

$$T_{\rm eff} = p_0 + p_1\,G_G + p_2\,(\mathrm{BP}-\mathrm{RP}) + p_3\,G_G\,(\mathrm{BP}-\mathrm{RP}) + p_4\,C_1 + p_5\,C_2. \quad (1)$$

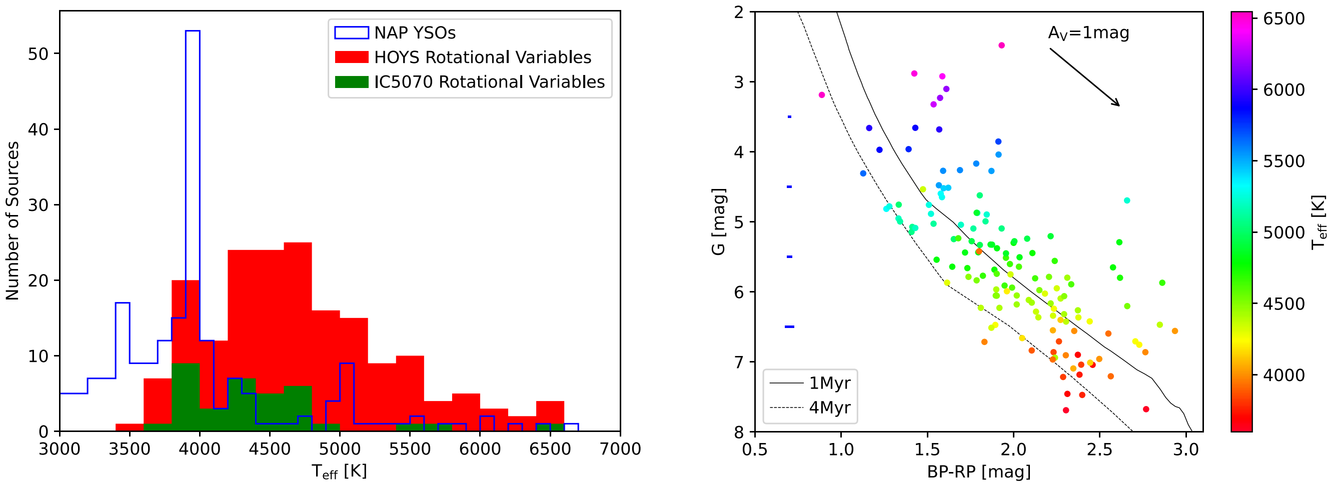

Figure 1. Left: In blue, we show the $T_{\rm eff}$ distribution of YSOs in the NAP region from M. Fang et al. (2020). In red, the distribution of the fitted $T_{\rm eff}$ values for the rotational variables in all HOYS fields is displayed, while in green the subsample of sources in IC 5070 is shown. Right: A *Gaia* colour versus absolute $G_{\rm mag}$ diagram of the rotational variables in our sample. The symbols are colour-coded with the fitted $T_{\rm eff}$ values. Typical *Gaia* colour errors are indicated as blue lines on the left-hand side. An extinction vector and 1 and 4 Myr PARSEC isochrones from A. Bressan et al. (2012) are overplotted for reference.

The $T_{\rm eff}$ distribution (blue histogram in the left panel of Fig. 1) of the M. Fang et al. (2020) NAP sample shows unusual peaks near 3500, 4000, and 5000 K, where objects appear to pile up, suggesting potential issues with these sources. We therefore fitted $T_{\rm eff}$ with and without these objects. Furthermore, because the sample contains far fewer high-temperature than low-temperature sources, we also performed the fitting with and without weighting each source (e.g. by $1/T_{\rm eff}$).

We used SCIPY (P. Virtanen et al. 2020) to obtain the best-fitting (lowest rms) parameters p_i for every combination of the two colours C_1 and C_2, with and without weighting and removal of objects in the $T_{\rm eff}$ peaks. All combinations yield very similar rms and $T_{\rm eff}$ values, with the worst rms only 10 per cent higher than the best. We therefore used all sources from M. Fang et al. (2020) without weighting, adopting $C_1 = K - W2$ and $C_2 = H - W1$ to fit $T_{\rm eff}$. These colours produce the lowest rms among those available for all investigated periodic variables.

The adopted colour combination includes the *WISE* bands, raising the possibility that infrared excess from circumstellar discs could bias the fitted $T_{\rm eff}$ values. However, testing all available colour combinations yields consistent temperatures within the uncertainties, with no systematic differences between objects with and without infrared excess (see Section 3.2). Likewise, although simultaneous fitting of extinction and $T_{\rm eff}$ would in principle be desirable, homogeneous and reliable extinction estimates are not available for the full sample. Since our calibration is empirical and based on spectroscopically determined $T_{\rm eff}$ values, any average reddening present in the calibration sample is implicitly incorporated into the fit. Moreover, as demonstrated in C. Herbert et al. (2023), systematic changes of several hundred Kelvin in $T_{\rm eff}$ alter the inferred spot temperatures by a comparable amount but have negligible effect on the spot coverages and do not change the distributions or conclusions presented here.

We show the distribution of the fitted values of $T_{\rm eff}$ for our sample of rotational variables as a red histogram in the left panel of Fig. 1 and list the values for all periodic sources in Table A1 in Appendix A. The $T_{\rm eff}$ distribution is much smoother than that of the M. Fang et al. (2020) sample and has no significant narrow peaks. It has a maximum at temperatures of about 4500 K, a much smaller fraction of objects below 4000 K, and a large population of higher temperature sources. This distribution is understandable in the context of the way these objects have been selected. They are from a mix of all HOYS target regions, which are at various distances of up to 1 kpc. The sources need to be sufficiently bright in the V-, R-, and I-band filters for their period and amplitudes to be measured. Thus, this sample is dominated by brighter, more massive stars than the NAP sample from M. Fang et al. (2020). For comparison, we overplotted the $T_{\rm eff}$ distribution for the sample of periodic variables in IC 5070. This accounts for about one-fifth of the entire HOYS sample.

The right-hand panel of Fig. 1 shows the entire sample in a *Gaia* colour versus absolute magnitude diagram, where the symbols are colour-coded based on the $T_{\rm eff}$ values. We also plot 1 and 4 Myr PAdova and tRieste Stellar Evolutionary Code (PARSEC) isochrones (A. Bressan et al. 2012) for reference, as well as a reddening vector. We can see that the fitted values of $T_{\rm eff}$ generally follow the expected trend with some outliers. Comparison with the overplotted PARSEC isochrones indicates that the sample of periodic variables consists predominantly of stars younger than about 4 Myr, with roughly half the sources lying above and half below the 1 Myr isochrone, implying a median age of approximately 1 Myr. Several sources are significantly above the 1 Myr isochrone. Thus, these are likely to be very young sources, unresolved higher-order multiples, objects affected by local nebulosity, or highly reddened objects.

The fitted values of $T_{\rm eff}$ and the observed sets of $\hat{A}^{o}_{\{V\}}$ values are used for each object and slice to fit the spot temperature and coverage with their uncertainties. These follow exactly the procedures outlined in C. Herbert et al. (2023, 2024). The only change made is that we extended the maximum spot temperature considered from 12 000 to 14 000 K. This was done due to some slightly higher effective temperature objects in our sample compared to our previous work in the IC 5070 field (C. Herbert et al. 2024). As demonstrated in appendix A of C. Herbert et al. (2023), systematic changes of a few hundred Kelvin in the adopted stellar $T_{\rm eff}$ result in approximately half that change in the fitted spot temperature,

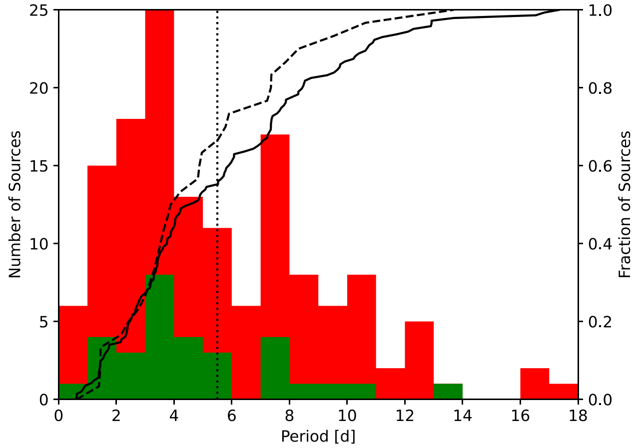

Figure 2. The period distribution of all rotational variables identified in the HOYS target fields is shown as a red histogram. The corresponding CDF is shown as a solid black line. The green histogram and the dashed CDF are the data for the objects in the IC 5070 field. The vertical dotted line separates fast and slow rotators.

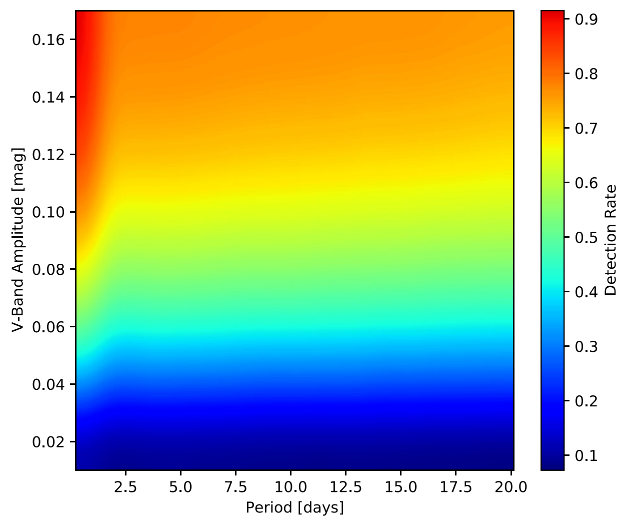

Figure 3. Simulated average detection rate in our data as described in Section 3.1 as a function of period and V-band amplitude.

while the inferred spot coverage changes by only a few per cent. These variations are well within the typical uncertainties of the spot fitting (about 300 K for the spot temperature and 15 per cent for the spot coverage) and therefore do not affect the spot property distributions discussed in this paper.

3 ROTATIONAL YSO SAMPLE CHARACTERIZATION

In this section, we discuss the stellar properties of the sample of rotational variables identified in all HOYS fields.

3.1 Period distribution

As shown in Section 2.3, we have reliably measured periods and amplitudes for 144 objects. The period distribution and the cumulative distribution function (CDF) are shown in Fig. 2. The distribution is clearly bimodal, in agreement with previous studies of solar-type stars (e.g. W. Herbst et al. 2002, 2007; M. V. Rodríguez-Ledesma et al. 2009, 2010; X.-L. Wang et al. 2023). The CDF suggests that the gap between the two peaks lies between 6 and 7 d. For consistency with our previous work (D. Froebrich et al. 2021; C. Herbert et al. 2023, 2024), we adopt 5.5 d as the boundary between fast and slow rotators. This yields 79 (55 per cent) fast rotators and 65 (45 per cent) slow rotators. Modest changes to this boundary do not significantly affect these fractions.

To assess potential biases in period detection, we performed injection–recovery simulations using our data. Artificial sinusoidal signals with periods between 0.75 and 19.6 d (in steps of 1.05 d) and V-band amplitudes from 0.02 to 0.16 mag (in steps of 0.02 mag) were added to all slices with sufficient data. The corresponding amplitudes in R and I were scaled by factors of 0.87 and 0.71, respectively, following C. Herbert et al. (2023). The signals were injected repeatedly with random phase, and the detection rate was recorded. As shown in Fig. 3, detection rates averaged over all objects depend primarily on amplitude and only weakly on period, decreasing by at most a few per cent across the period range considered. This reflects the fact that periods up to 20 d are sampled within ∼180 d windows, so the reduced number of cycles at longer periods has only a minor impact on detectability.

Table 2. Number and fraction of fast/slow rotators and $K-W2$ excess sources in selected HOYS target fields, sorted by increasing fraction of slow rotators. See text for details on how the fields are defined. Note that the numbers in the row 'Total' include the sum of sources in the entire HOYS sample.

Region	Fast rotators		Slow rotators		E($K-W2$)	
	N	(per cent)	N	(per cent)	N	(per cent)
Orion	30	71	12	29	9	21
IC 5070	20	65	11	35	17	55
IC 1396	19	45	23	55	9	21
σ Ori	2	12	15	88	7	41
Total	79	55	65	45	50	35

Since the period distribution combines multiple HOYS regions, we examine variations between fields. The most populated region, IC 5070, previously studied in D. Froebrich et al. (2021) and C. Herbert et al. (2023, 2024), is overplotted in Fig. 2. We find 20 (65 per cent) fast and 11 (35 per cent) slow rotators, consistent with earlier results and indicating a slightly higher fraction of fast rotators than in the full sample. For most other regions, small number statistics limit direct comparisons. However, combining spatially related fields yields more robust estimates (Table 2). We group IC 1396 A and N into 'IC 1396', and M42, L1641 N, V898 Ori, YY Ori, and V555 Ori into 'Orion', while σ Ori is treated separately. Despite the diversity of environments, the fast/slow fractions are broadly consistent: Orion and IC 5070 show roughly two-thirds fast and one-third slow rotators, while IC 1396 is close to an even split. Though the statistics are poor for the σ Ori region, it stands out with nearly 90 per cent of its 14 objects being slow rotators and (as discussed in the next subsection) about 40 per cent exhibiting a $K-W2$ excess.

3.2 Inner disc excess

The bimodality of YSO rotation periods is commonly attributed to disc braking, where magnetic coupling between the star and its inner disc regulates angular momentum (e.g. J. Bouvier et al. 2014; L. Venuti et al. 2017; Y. Bu et al. 2025). We therefore use the $K - W2$ colour to identify the inner dust discs in our sample. Objects with excess emission in this colour (>0.5 mag) are interpreted as hosting warm dust close to the star, indicative of a dense inner disc (P. S. Teixeira et al. 2012), or a thick disc.

The disc excess fraction for the full sample and the four regions defined previously is summarized in Table 2. Overall, one third of the objects show a $K - W2$ excess. We note that the absence of excess does not imply the absence of an inner disc, as dust-depleted or anaemic discs (e.g. P. S. Teixeira, A. Scholz & J. Alves 2020) remain undetected in this colour. The disc fraction varies from ∼20 per cent in Orion and IC 1396 to 40 per cent in σ Ori and just over 50 per cent in IC 5070, consistent with D. Froebrich et al. (2024) despite the more stringent variability selection applied here.

The relation between rotation period and $K - W2$ colour is shown in the top panel of Fig. 4, where vertical and horizontal lines at 5.5 d and 0.5 mag separate fast/slow rotators and disc/no-disc objects, respectively. About 40 per cent of the sample are fast rotators without disc excess, while the 45 per cent of slow rotators split evenly between disc-bearing and disc-free systems. In the standard disc braking picture, stars evolve from slow rotators with discs to fast rotators without discs. However, about one fifth of the sample consists of slow rotators without detectable dust discs, possibly due to gas-rich but dust-depleted discs or tidal locking in binaries. Conversely, roughly 15 per cent of objects are fast rotators with disc excess, which may reflect binarity or weaker magnetic coupling. Colour-coding by region shows that slow rotators without disc excess are rare in IC 5070 and are predominantly found in Orion and IC 1396.

The middle and bottom panels of Fig. 4 show the spectral energy distribution (SED) slope $\alpha_{\rm SED}$, derived from the $W1$ to $W4$ *WISE* magnitudes following D. Majaess (2013), as a function of the rotation period and $K - W2$, respectively. The nominal boundaries between Class 1 and Class 2 ($\alpha_{\rm SED} = 0$) and between Class 2 and Class 3 ($\alpha_{\rm SED} = -2$) are indicated. The sample is dominated by Class 2 objects, with few Class 1 or Class 3 sources. Within the Class 2 population, objects with disc excess tend to have higher $\alpha_{\rm SED}$ values. A threshold at $\alpha_{\rm SED} = -1$ separates Class 2 objects with and without inner dust discs, which we refer to as early and late Class 2. Accordingly, 70 per cent of early Class 2 objects show disc excess, while 85 per cent of late Class 2 objects do not. With the exception of very short rotation periods ($P < 2$ d), the $\alpha_{\rm SED}$ slope shows no correlation with the rotation period of the source. This suggests that the innermost parts of the disc are the dominant component regulating angular momentum transfer. Once a small [fraction of an au (astronomical unit)] hole is present in the inner disc, the star may no longer be efficiently coupled to the disc, irrespective of how much material remains at larger radii.

The *Gaia* colour–magnitude diagram of the sample is shown in Fig. 5, using absolute magnitudes derived from inverted parallaxes without extinction correction. PARSEC isochrones for 1 and 4 Myr (A. Bressan et al. 2012) are overplotted. Colour coding by period–disc classification (left panel) and region (right panel) reveals no clear trends: objects with and without disc excess are not separated, and neither population is preferentially associated

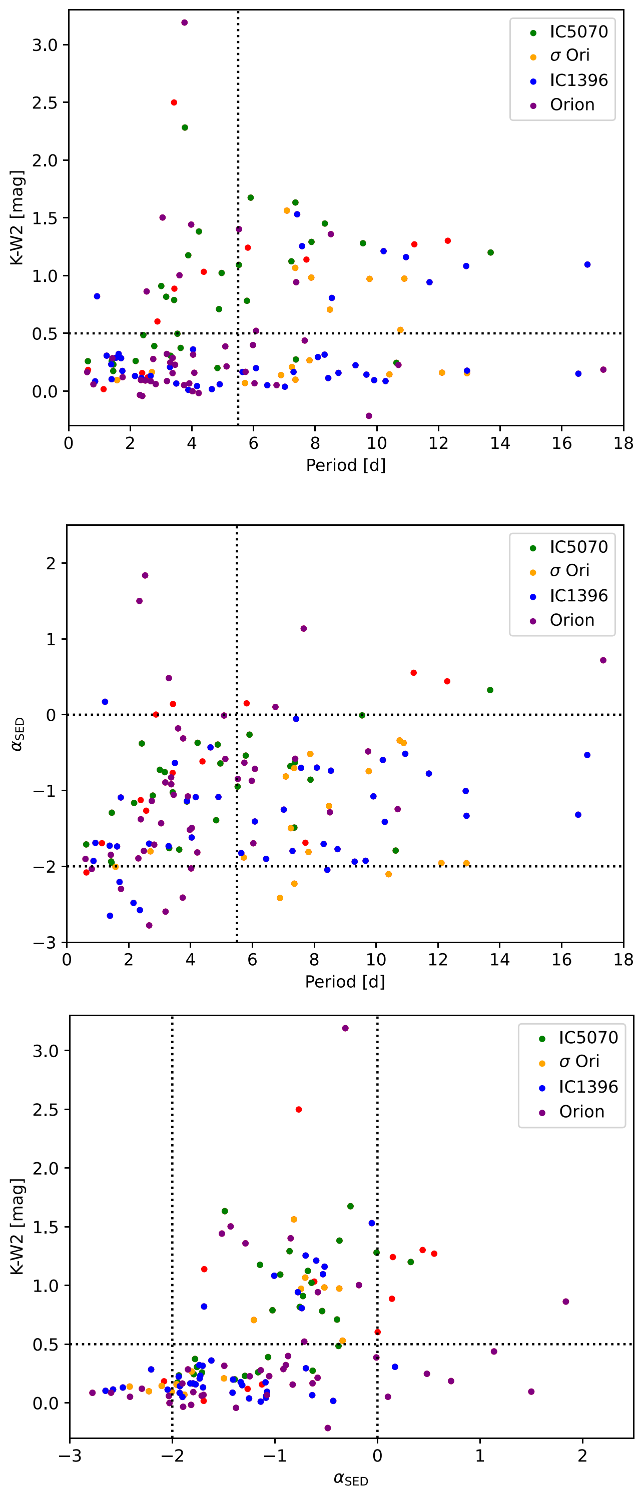

Figure 4. Relationship between the period, $K - W2$ colour, and $\alpha_{\rm SED}$ slope for the rotational variables in our sample. The colour code indicates the region the sources are in. Red dots indicate objects not in any of the four populous regions. Dotted lines separate fast and slow rotators at $P = 5.5$ d, sources with and without colour excess at $K - W2 = 0.5$ mag, and Class 1, 2, and 3 objects based on their $\alpha_{\rm SED}$ value. Top: The rotation period versus the $K - W2$ colour. Middle: The rotation period versus the $\alpha_{\rm SED}$ slope. Bottom: The $K - W2$ colour versus the $\alpha_{\rm SED}$ slope.

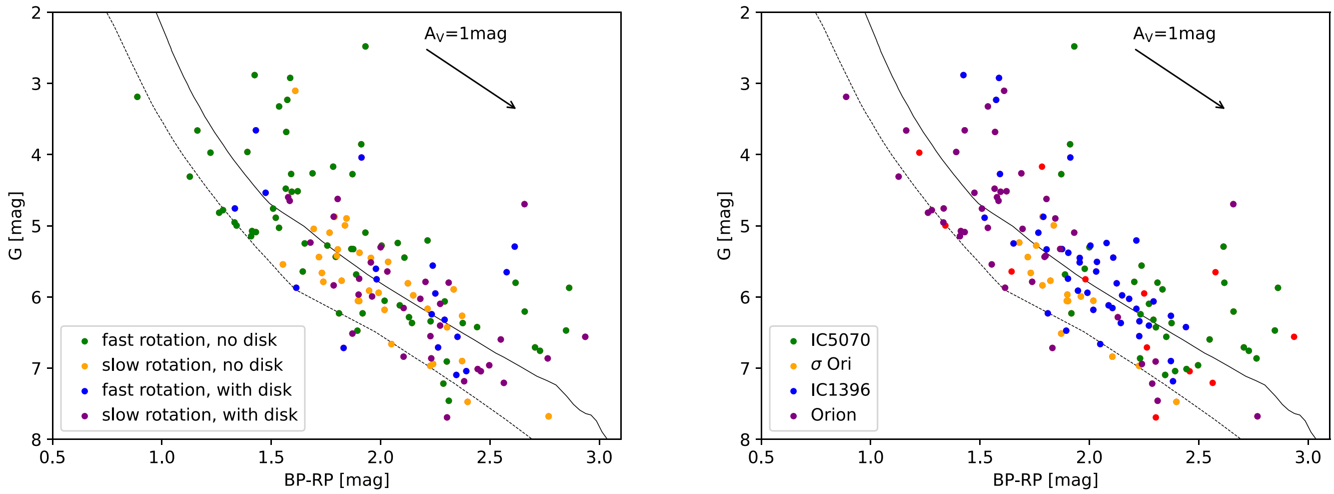

Figure 5. *Gaia* absolute magnitude versus colour of the rotational variables. In the left panel, the objects are colour-coded based on their distribution in the period versus $K-W2$ colour plot, and in the right panel according to the star formation region they are in. In all panels, the solid black line is a 1 Myr PARSEC isochrone and the dashed black line a 4 Myr isochrone (A. Bressan et al. 2012).

with younger or older isochrones or specific regions. The lower mass limit corresponds to $G \approx 7$ mag, i.e. $\sim$0.6 M$_\odot$ at 4 Myr (A. Bressan et al. 2012).

Brighter stars ($G < 5$ mag, $>$1 M$_\odot$) are predominantly found in Orion, while lower-mass objects are more common in IC 5070. These brighter stars are mainly fast rotators without disc excess; 65 per cent fall into this category. This is consistent with more massive stars dispersing their inner discs more rapidly through stronger radiation (J. M. Carpenter et al. 2006), leading to earlier spin-up.

3.3 Rotational variables – summary

We have identified a sample of 144 rotationally variable YSOs from 12 different HOYS target fields (young star clusters/star-forming regions). Their placement in the colour–magnitude diagram suggests that they are mainly younger than 4 Myr, with a median age of about 1 Myr. Their estimated effective temperatures range from 3500 to 6500 K, placing them in an approximate mass range of 0.6 to 2 M$_\odot$. The sample is dominated by Class 2 objects, and one third shows excess emission that can be attributed to warm dust in the inner disc. This supports the standard disc braking scenario in which slow rotators preferentially retain discs while fast rotators are typically disc-free. However, substantial populations of slow rotators without dust excess and fast rotators with discs indicate that additional effects such as gas-rich dust-depleted discs, binarity, or weaker magnetic coupling also influence rotational evolution. Two-thirds of the sample are fast rotators, predominantly without disc excess emission. The hotter stars (above 5000 K) are generally fast rotators without disc excess emission. There are no discernible age trends with rotation period, disc excess, or location.

4 CHARACTERIZATION OF SPOT PROPERTIES

4.1 Method comparison in IC 5070

In the following sections, we discuss the distributions of spot properties derived for our sample, based on amplitude measurements of periodic light curves and fitted stellar effective temperatures. We follow the spot-fitting procedures outlined in C. Herbert et al. (2023, 2024) with very minor adjustments discussed in Section 2.4. In C. Herbert et al. (2024), the spot properties in IC 5070 were determined using measured $T_{\rm eff}$ values from M. Fang et al. (2020). Here, we first compare those results with the updated $T_{\rm eff}$ distributions obtained in this work.

Fig. 6 shows histograms and CDFs of spot coverage and spot–star temperature differences ($T_{\rm S} - T_\star$) for warm (left) and cold (right) spots, derived using three approaches. Sample 1 (red) corresponds to C. Herbert et al. (2024). Sample 2 (green) uses the same amplitudes but updated fitted $T_{\rm eff}$ values, while sample 3 (blue) represents the full analysis of this work, including minor amplitude differences caused by small changes in the start dates of light-curve slices. The general distributions are consistent, with small systematic offsets mainly due to the systematically higher $T_{\rm eff}$ values adopted here.

For cold spots, the temperature difference between the spot and the star increases by $\sim$200 K, approximately half the typical increase in $T_{\rm eff}$, consistent with the simulations in C. Herbert et al. (2023). The cold spot coverage decreases by $\sim$0.01 when using the fitted $T_{\rm eff}$. The small differences between samples 2 and 3 indicate that the correspondingly small differences in the measured amplitudes do not significantly affect the derived spot property distributions. Thus, the updated $T_{\rm eff}$ values introduce only small systematic shifts, comparable to the typical uncertainties, while providing a more realistic $T_{\rm eff}$ distribution (left panel of Fig. 1) and more reliable cold spot properties.

For warm spots, the changes are smaller and less systematic. The temperature difference increases again slightly ($\sim$200 K) when using the fitted $T_{\rm eff}$ values, while the coverage distribution remains largely unchanged. Variations in amplitude measurements have a somewhat larger effect, producing a slightly higher fraction of large warm spots. However, these are few in number, and their properties are less certain (see Section 4.2.3).

The distributions of spot coverage and temperature difference for the full sample are shown in the left panel of Fig. 7, with histograms and CDFs of spot coverage for cold and warm spots in the right panel. These are discussed in the following subsections.

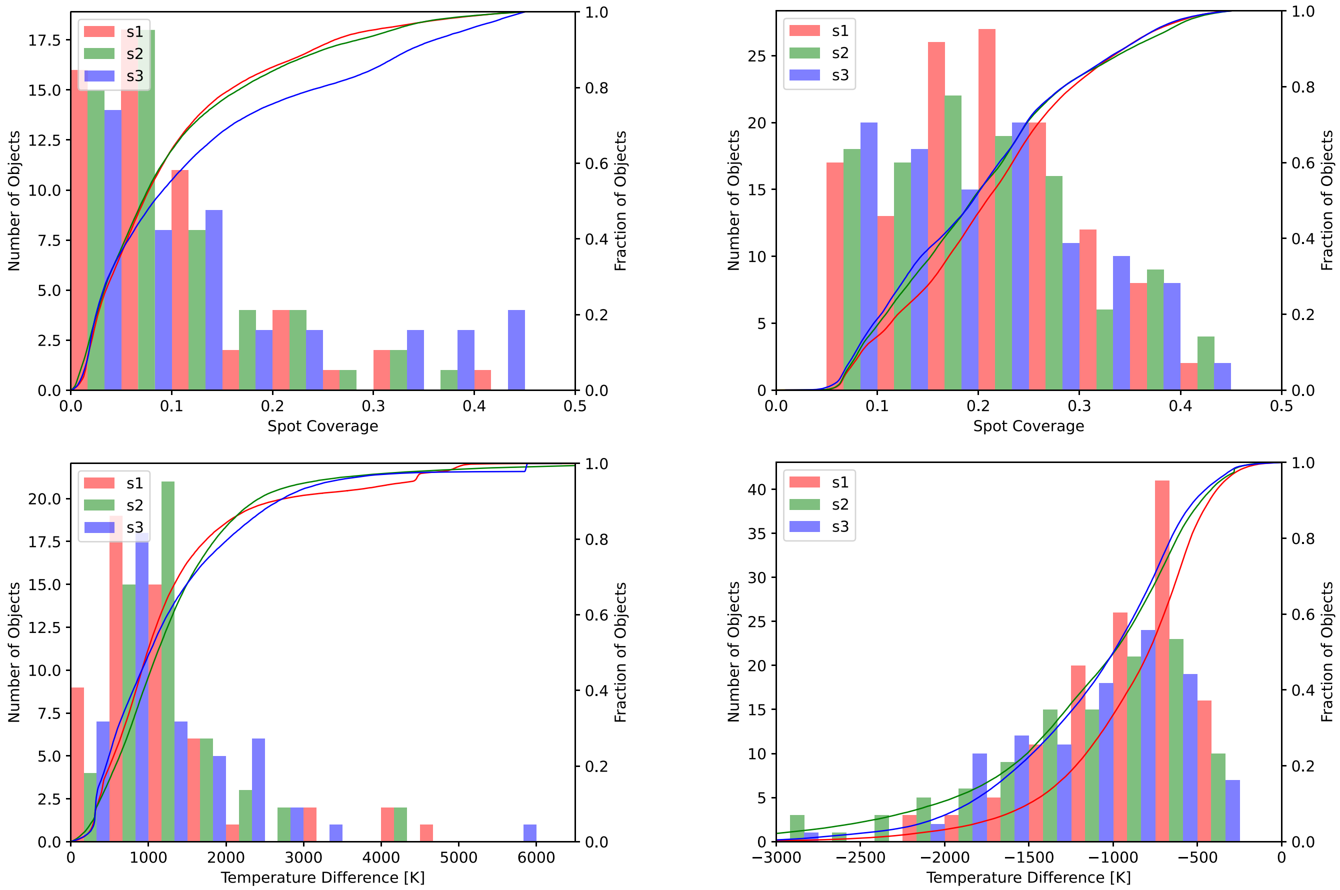

Figure 6. Comparison of spot property distributions from C. Herbert et al. (2024) and this work for IC 5070. Sample 1 is the original sample from C. Herbert et al. (2024). In sample 2, we used the same amplitudes but our fitted values of $T_{\rm eff}$. Sample 3 represents this work. Warm spot properties are in the left column, and cold spot properties are in the right column. The top row shows the coverage distribution, and the bottom row shows the star–spot temperature difference distribution.

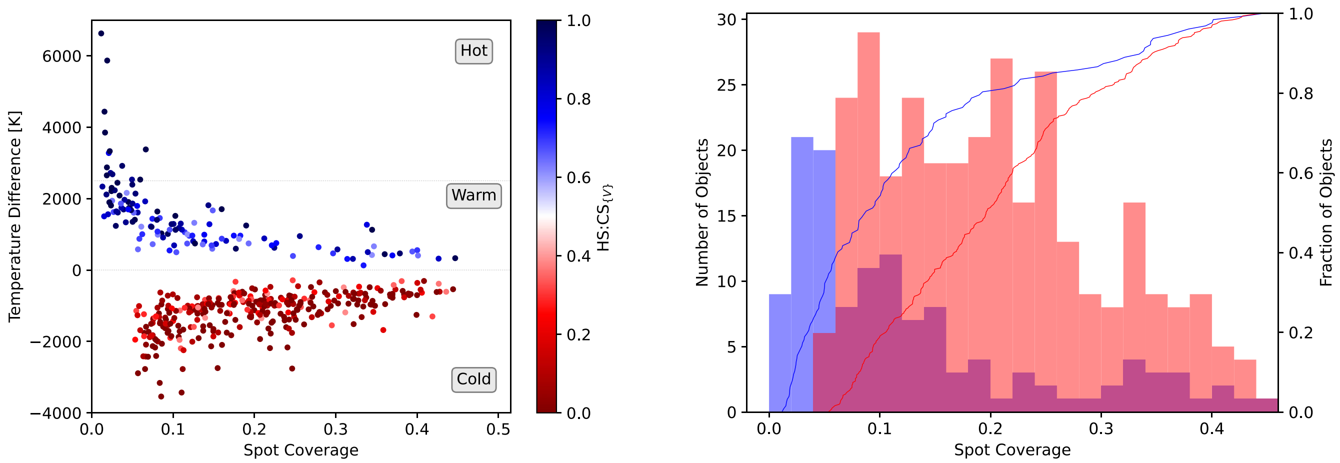

Figure 7. Left: Spot temperature difference $T_{\rm S} - T_\star$ versus spot coverage for the entire sample of rotational variables. Horizontal dotted lines mark $T_{\rm S} - T_\star = 0$ K and $T_{\rm S} - T_\star = 2500$ K, which separate the cold, warm, and hot spot solutions. The symbols are colour-coded according to the HS:CS$_{\{V\}}$ ratio, our spot property quality indicator. Values close to zero indicate well-constrained cold spot properties. Values near 1 indicate well-constrained warm/hot spot properties. Values near 0.5 correspond to increasingly degenerate hot and cold spot solutions (see C. Herbert et al. 2024, for details). The typical uncertainties of the spot coverage and temperature differences are 0.02 and 250 K, respectively. Right: Distribution of spot coverage of hot/warm (blue) and cold spots (red). The solid lines are the CDFs of the hot/warm (blue) and the cold spots (red).

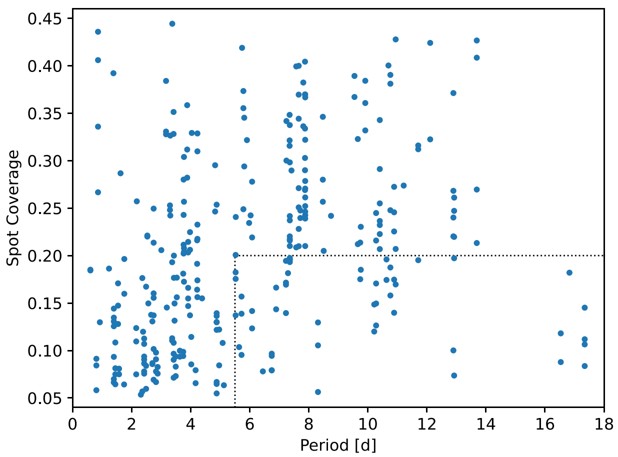

Figure 8. Stellar rotation periods versus the coverage for all cold spots in our sample. A lack of small spots on slow rotators is evident (bounded by the black dotted lines). The typical uncertainties of the spot coverage are 0.02. The period uncertainties are typically smaller than the symbol size.

4.2 Cold spot properties

The distribution of cold spot coverage (red histogram in the right panel of Fig. 7) is very similar to that found for IC 5070 in C. Herbert et al. (2024), showing an approximately flat distribution between the detection limit (coverage of 0.05) and ≈0.25. To recover the underlying true distribution, this observed distribution must be corrected for the detection efficiency of our method using the simulations described in Section 3.1 (see also Fig. 3). This is addressed in Section 4.2.3. Before doing so, we assess whether additional selection effects or biases could influence the observed distribution.

The key feature of the data is the dependence of spot coverage on the rotation period (Fig. 8). The fast rotator population ($P < 5.5$ d) contains a much higher fraction of low coverage spots and very few large coverage spots. On the other hand, slow rotators ($P > 5.5$ d) are dominated by large spot coverage (>0.20), with comparatively few small spots. This behaviour is not expected from detection biases. The simulations in Fig. 3 demonstrate that the detection rate is essentially independent of the rotation period. Hence, the observed trend is likely physical, reflecting a combination of shorter lifetimes, non-existence of small spots, and/or smaller temperature contrasts for low-coverage spots on slow rotators. There are two main explanations for why small cold spots could not exist on the slow rotators. The magnetic pressure on the spatial scale of the spots is lower than the gas pressure in the surrounding stellar atmosphere. The granulation scale on the stars is larger than the spot size. Both are very unlikely given the nature of the YSOs and the coverage range (0.05–0.20) of the ‘missing’ cold spots.

We briefly consider and exclude other possible explanations. The simulations rule out a detection bias against low-coverage spots at longer periods. A bias in the effective temperature is also unlikely. When we restrict the sample to $T_{\rm eff} < 5500$ K (where both fast and slow rotators are present), it does not alter the observed distribution. Thus, the $T_{\rm eff}$ distribution cannot account for the trend. Consistent with studies of main-sequence stars, where larger spots and spots on cooler stars have longer lifetimes (H. A. C. Giles, A. Collier Cameron & R. D. Haywood 2017), the most plausible explanations are that low-coverage spots on slow rotators either have reduced temperature contrast, or have lifetimes too short to be detected by our methodology. These will be briefly discussed in the next two subsections. Furthermore, using homogeneous period and coverage distributions, a simple Monte Carlo simulation shows that there is less than 6×10^{-5} chance that the observed distribution is a statistical fluke.

4.2.1 *Cold spot temperature contrast*

The key result is that variations in the spot–star temperature contrast cannot explain the lack of low-coverage spots on slow rotators. As shown in the left panel of Fig. 7, there is a weak trend in the cold spot properties: spots with large temperature differences (>2000 K) predominantly have small coverage. This implies that smaller spots tend to exhibit higher temperature contrasts than larger cold regions. We note that the derived spot temperatures represent averages over the full spot area, and localized regions within the spots may reach lower temperatures.

There is a detection bias, as the sensitivity to spot–star temperature differences increases with spot coverage. For a given temperature contrast, larger spots produce higher amplitudes and are therefore easier to detect. To account for this, we impose a common lower limit on the temperature difference (e.g. 750 K). This slightly modifies the period-coverage distribution, but does not remove the main trend. In particular, the deficit of low-coverage spots among slow rotators persists, as the selection primarily removes larger spots across all periods. Hence, while reduced temperature contrasts contribute to the observed behaviour in Fig. 8, they are not the dominant effect.

4.2.2 *Cold spot lifetimes*

Our period determination (Section 2.3) is based on 6-month light-curve segments. As a result, only spots that remain stable for a significant fraction of this time-scale can be detected. In practice, this implies that only spots with lifetimes $\gtrsim$150–200 d are included in our analysis. The absence of small spots on slow rotators (Fig. 8) therefore directly indicates that such spots must have lifetimes shorter than this threshold and are therefore not recovered by our method. In combination with the lack of biases discussed above, this strongly suggests that spot lifetime is the primary driver of the observed distribution.

This interpretation can be placed in the framework of turbulent magnetic diffusivity. S. J. Bradshaw & P. Hartigan (2014) showed that the empirical spot lifetime–size relation can be explained if the relevant diffusion scale is set by the supergranule size, with only a weak dependence on other stellar parameters. Using their fig. 1, we can estimate whether our results are consistent with this picture. For fast rotators, the detection limit of a coverage of 0.05 corresponds to spot radii of about $1.5\text{–}2.2 \times 10^5$ km (assuming single spots on stars with radii of 1–1.5 $R_\odot$). These spots persist for at least 150–200 d, which implies supergranule sizes of $\lesssim 0.1\,R_\odot$. In contrast, for slow rotators, spots with coverage <0.2 (radii about $3.0\text{–}4.5 \times 10^5$ km) are rarely detected, indicating lifetimes shorter than 6 months. Within the same framework, this implies substantially larger supergranules, of the order of half the solar radius or more.

These results suggest that spot lifetimes, and hence supergranule sizes, depend on stellar rotation. Faster rotating stars appear to host smaller supergranules, allowing spots of a given size to

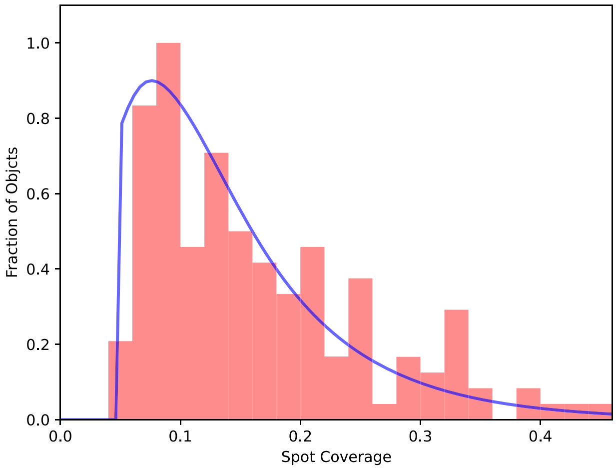

Figure 9. Exponential fit to the coverage distribution of cold spots on fast rotators. The fit has been corrected for the detection efficiency shown in Fig. 3.

survive longer. This is consistent with the established proportionality between spot size and lifetime for the Sun and main-sequence stars (M. N. Gnevyshev 1938; M. Waldmeier 1955; K. Petrovay & L. van Driel-Gesztelyi ; S. V. Berdyugina 2005), and likely extends to YSOs (see also H. A. C. Giles et al. 2017). We note that our measurements represent asymmetrically distributed spot coverage rather than individual spot sizes, and thus the inferred radii are upper limits.

In summary, the lack of small spots on slow rotators is best explained by short spot lifetimes below ~6 months. Within the turbulent diffusivity framework, this implies that supergranule sizes decrease during the spin-up phase after disc dispersal, potentially by at least a factor of 5. The physical origin of supergranule sizes remains uncertain even for the Sun (S. J. Bradshaw & P. Hartigan 2014), but the apparent dependence on rotation suggests a link to changes in magnetic field structure during early stellar evolution. A more detailed analysis of spot lifetimes as a function of coverage and rotation is required to quantify this effect, but this is beyond the scope of this work.

4.2.3 *Cold spot coverage distribution*

In Fig. 7, we present the distribution of spot properties for the full sample, extending fig. 5 of C. Herbert et al. (2024) to a sample ~2.5 times larger. As shown in the previous subsection, the spot coverage distribution depends on rotation period, with only fast rotators ($P < 5.5$ d) hosting spots whose lifetimes exceed the 6-month detection limit across the full coverage range. We therefore restrict the analysis of the intrinsic coverage distribution to these objects (Fig. 9).

The observed distribution peaks at a coverage just below 0.1, and at a star–spot temperature difference near 1000 K (not shown). After correcting for detection efficiency using the simulations described in Section 3.1 (see also Fig. 3), we test different functional forms for the underlying spot coverage distribution. Lognormal and power-law models fail to reproduce the data, while an exponential distribution provides a good fit (solid blue line in Fig. 9). This demonstrates that small spot coverages are intrinsically much more common than large ones, with no preferred coverage beyond a characteristic scale. Such behaviour is naturally explained if spot formation is governed by stochastic magnetic flux emergence rather than by a process that produces a characteristic spot size. The temperature contrast distribution cannot be modelled in the same way because the rise towards the peak at ~1000 K is strongly affected by selection effects. However, beyond this peak the number of spots decreases rapidly with increasing temperature contrast, qualitatively consistent with stronger suppression of convection being progressively less common.

For slow rotators ($P > 5.5$ d), the observed distribution peaks at a coverage of ~0.2 and a temperature difference just below 1000 K, consistent with the lifetime-driven detection bias discussed above. However, the number statistics are insufficient to constrain the underlying distribution for this subsample.

4.3 Hot/warm spot properties

The coverage distribution of hot/warm spots indicates the presence of two distinct populations (right panel in Fig. 7). The distribution is bimodal, with peaks near 0.05 and 0.1, implying two approximately equally populated groups: small hot spots consistent with accretion column footprints, and larger warm spots likely associated with plages or faculae.

There are significantly fewer hot/warm spots (128) than cold spots (311) in our sample. In addition, some solutions for large coverage, warm spots are less reliable, as indicated by low HS:CS$_V$ values (see C. Herbert et al. 2024 for details). Consequently, the following discussion remains qualitative. C. Herbert et al. (2024) reported an apparent gap between the hot and the warm spots in the spot–star temperature difference distribution. With the improved sample size, this gap is no longer present. Instead, the temperature distribution is smooth. Unlike for cold spots, there is no clear deficit of small warm/hot spots on slow rotators, although this may be influenced by limited number statistics.

The larger warm spots identified are consistent with magnetic surface features such as plages or faculae (see also D. Froebrich et al. 2020). If this interpretation is correct, these structures should have a latitude distribution similar to that of the cold spots. However, confirming this would require detailed modelling of phase-folded light curves, which is beyond the scope of this work.

5 CONCLUSION

We conducted the first homogeneous, multiregion analysis of rotational variability and spot properties in YSOs using long-term, multiband photometry from the HOYS project. From an initial sample of over 2000 candidate members across 25 star-forming regions, we identified 144 YSOs with robust periodic signals and well-constrained amplitudes in three optical bands. These objects span 12 regions and occupy a well-defined locus in colour–magnitude space consistent with ages younger than ~4 Myr, with a typical age of the order of 1 Myr. Their effective temperatures range from approximately 3500 to 6500 K, corresponding to a mass range of roughly 0.6–2 M$_\odot$. The sample is dominated by Class 2 objects, with about one third showing clear evidence of warm dust in the inner disc.

The distribution of rotation periods is strongly bimodal, with 55 per cent of the objects classified as fast rotators ($P < 5.5$ d) and 45 per cent as slow rotators. This bimodality is robust against observational biases and is consistently recovered across multiple regions, in agreement with previous work. The relationship between rotation and inner disc indicators supports the disc-braking paradigm: fast rotators are predominantly discless, while slow rotators comprise both disc-bearing and disc-free systems. At the same time, the presence of slow rotators without detectable dust discs and fast rotators with disc signatures demonstrates that disc braking alone cannot fully account for the observed rotational states, highlighting the role of additional physical processes such as magnetic field strength, binarity, or rapid disc evolution.

By combining multiband amplitudes with photometrically derived effective temperatures, we have characterized the statistical properties of stellar spots across this diverse sample. For fast rotators, the intrinsic cold spot coverage distribution is well described by an exponential function once observational biases are removed. This implies that small spot coverages are intrinsically much more common than large ones and suggests that spot formation is governed by stochastic magnetic flux emergence rather than by a process producing a preferred spot size. This constitutes the first empirical constraint on the intrinsic spot coverage distribution of YSOs. In contrast, slow rotators show a pronounced deficit of small-coverage spots. Given that our simulations demonstrate a negligible dependence of detectability on rotation period, this difference is intrinsic and points to a fundamental change in spot evolution between the populations of fast and slow rotators. The inferred spot property distributions are robust against plausible systematic uncertainties in the adopted stellar effective temperatures and other methodological choices discussed in Section 2.4, indicating that the conclusions presented here do not depend on the precise temperature calibration.

The most significant result of this work is that spot evolution differs fundamentally between fast and slow rotators. The absence of small, long-lived spots on slow rotators suggests that these features evolve or decay on time-scales shorter than the 6-month window required for detection, while comparable spots on fast rotators remain stable. Within the framework of turbulent magnetic diffusion, this implies that the characteristic scales of surface convection, and therefore magnetic structuring, differ significantly between fast and slow rotators. In other words, our data suggest that the supergranule sizes in YSOs are influenced by the rotation period. Although this interpretation relies on indirect inference, the consistency of the observed trends across the sample provides compelling evidence for a rotation-dependent regime of magnetic surface structure in young stars.

Warm and hot spot solutions reveal a more complex picture, with indications of two distinct populations: small, high-temperature contrast features consistent with accretion funnel footprints, and larger, moderate-temperature structures that may represent plage- or faculae-like activity. Although the number statistics are limited, these results suggest that both magnetic activity and accretion processes contribute to the observed rotational variability in YSOs.

Together, our results establish an observational picture in which rotation, disc evolution, and magnetic surface structure are closely linked in young stars. The combination of a bimodal rotation distribution, a partially, but not exclusively, disc-regulated spin evolution, and a rotation-dependent cold spot coverage distribution provides new empirical constraints on models of early stellar angular momentum evolution and magnetic activity. Future work incorporating improved stellar parameter estimates, extinction corrections, and time-resolved spot modelling will be essential to refine these conclusions and to fully exploit the unique long-term monitoring capabilities of the HOYS survey.

ACKNOWLEDGEMENTS

We would like to thank all contributors of observational data for their efforts towards the success of the Hunting Outbursting Young Stars (HOYS) project. CH was supported by the Science and Technology Facilities Council under grant number STFC Kent 2020 DTP ST/V50676X/1. HS-G was supported by the Science and Technology Facilities Council under grant number STFC Kent ST/Y509267/1.

DATA AVAILABILITY

The data underlying this article are available in the HOYS data base at https://astro.kent.ac.uk/HOYS-CAPS/.

REFERENCES

Audard M. et al., 2014, in Beuther H., Klessen R. S., Dullemond C. P., Henning T., eds, Protostars and Planets VI. Univ. Arizona Press, Tucson, AZ, p. 387
Babcock H. W., 1961, ApJ, 133, 572
Belloche A., 2013, in Hennebelle P., Charbonnel C., eds, EAS Publ. Ser. Vol. 62, Role and Mechanisms of Angular Momentum Transport During the Formation and Early Evolution of Stars. EDP Sciences, Les Ulis, France, p. 25 10.1051/eas/1362002
Berdyugina S. V., 2005, Living Rev. Sol. Phys., 2, 8
Bouvier J. et al., 1999, A&A, 349, 619
Bouvier J., Matt S. P., Mohanty S., Scholz A., Stassun K. G., Zanni C., 2014, in Beuther H., Klessen R. S., Dullemond C. P., Henning T., eds, Protostars and Planets VI. Univ. Arizona Press, Tucson, AZ, p. 433
Bozhinova I., Scholz A., Eislöffel J., 2016, MNRAS, 458, 3118
Bradshaw S. J., Hartigan P., 2014, ApJ, 795, 79
Bressan A., Marigo P., Girardi L., Salasnich B., Dal Cero C., Rubele S., Nanni A., 2012, MNRAS, 427, 127
Bu Y., He C., Fang M., Li C., 2025, ApJ, 979, 29
Carpenter J. M., Hillenbrand L. A., Skrutskie M. F., 2001, AJ, 121, 3160
Carpenter J. M., Mamajek E. E., Hillenbrand L. A., Meyer M. R., 2006, ApJ, 651, L49
Cody A. M. et al., 2014, AJ, 147, 82
Cody A. M., Hillenbrand L. A., David T. J., Carpenter J. M., Everett M. E., Howell S. B., 2017, ApJ, 836, 41
Cutri R. M. et al., 2013, VizieR On-line Data Catalog: II/328. Originally published in: IPAC/Caltech (2013)
Espaillat C. C., Robinson C. E., Romanova M. M., Thanathibodee T., Wendeborn J., Calvet N., Reynolds M., Muzerolle J., 2021, Nature, 597, 41
Evitts J. J. et al., 2020, MNRAS, 493, 184
Fallscheer C., Herbst W., 2006, ApJ, 647, L155
Fang M., Hillenbrand L. A., Kim J. S., Findeisen K., Herczeg G. J., Carpenter J. M., Rebull L. M., Wang H., 2020, ApJ, 904, 146
Fischer W. J., Hillenbrand L. A., Herczeg G. J., Johnstone D., Kospal A., Dunham M. M., 2023, in Inutsuka S.-i., Aikawa Y., Muto T., Tomida K., Tamura M., eds, ASP Conf. Ser. Vol. 534, Protostars and Planets VII. Astron. Soc. Pac., San Francisco, p. 355
Froebrich D. et al., 2018, MNRAS, 478, 5091
Froebrich D., Scholz A., Eislöffel J., Stecklum B., 2020, MNRAS, 497, 4602
Froebrich D. et al., 2021, MNRAS, 506, 5989
Froebrich D. et al., 2024, MNRAS, 529, 1283
Gaia Collaboration, 2016, A&A, 595, A1
Gaia Collaboration, 2023, A&A, 674, A1
Gallet F., Zanni C., Amard L., 2019, A&A, 632, A6
Giles H. A. C., Collier Cameron A., Haywood R. D., 2017, MNRAS, 472, 1618
Gnevyshev M. N., 1938, Izvestiya Glavnoj Astron. Obs. Pulkove, 16, 36
Grankin K. N., Bouvier J., Herbst W., Melnikov S. Y., 2008, A&A, 479, 827
Hale G. E., Ellerman F., Nicholson S. B., Joy A. H., 1919, ApJ, 49, 153

Herbert C., Froebrich D., Scholz A., 2023, MNRAS, 520, 5433
Herbert C. et al., 2024, MNRAS, 529, 4856
Herbst W., Bailer-Jones C. A. L., Mundt R., Meisenheimer K., Wackermann R., 2002, A&A, 396, 513
Herbst W., Eislöffel J., Mundt R., Scholz A., 2007, in Reipurth B., Jewitt D., Keil K., eds, Protostars and Planets V. Univ. Arizona Press, Tucson, AZ, p. 297
Ingleby L. et al., 2013, ApJ, 767, 112
Johns-Krull C. M., 2007, ApJ, 664, 975
Koenigl A., 1991, ApJ, 370, L39
Lawrence A. et al., 2007, MNRAS, 379, 1599
Li J., 2018, ApJ, 867, 89
Lightfoot J. F., 1989, MNRAS, 239, 665
Lucas P. W. et al., 2008, MNRAS, 391, 136
Majaess D., 2013, Ap&SS, 344, 175
Matt S., Pudritz R. E., 2005, ApJ, 632, L135
Morris B. M., 2020, ApJ, 893, 13
Petrovay K., van Driel-Gesztelyi L., 1997, Sol. Phys., 176, 249
Reipurth B., Jewitt D., Keil K., eds, 2007, Protostars and Planets V. Univ. Arizona Press, Tucson, AZ
Rodríguez-Ledesma M. V., Mundt R., Eislöffel J., 2009, A&A, 502, 883
Rodríguez-Ledesma M. V., Mundt R., Eislöffel J., 2010, A&A, 515, A13
Scholz A., Stelzer B., Costigan G., Barrado D., Eislöffel J., Lillo-Box J., Riviere-Marichalar P., Stoev H., 2012, MNRAS, 419, 1271
Sicilia-Aguilar A., Hartmann L. W., Fürész G., Henning T., Dullemond C., Brandner W., 2006, AJ, 132, 2135
Sicilia-Aguilar A. et al., 2023, MNRAS, 526, 4885
Skrutskie M. F. et al., 2006, AJ, 131, 1163
Stauffer J. et al., 2016, AJ, 151, 60
Teixeira P. S., Lada C. J., Marengo M., Lada E. A., 2012, A&A, 540, A83
Teixeira P. S., Scholz A., Alves J., 2020, A&A, 642, A86
Venuti L. et al., 2017, A&A, 599, A23
Virtanen P. et al., 2020, scipy/scipy: SciPy 1.6.0 (Version v1.6.0) [Computer software]. Zenodo. https://doi.org/10.5281/zenodo.4406806
Waldmeier M., 1955, Ergebnisse und Probleme der Sonnenforschung. Geest & Portig, Leipzig
Wang X.-L., Fang M., Herczeg G. J., Gao Y., Tian H.-J., Zhou X.-Y., Zhang H.-X., Chen X.-P., 2023, Res. Astron. Astrophys., 23, 075015
Zanni C., Ferreira J., 2013, A&A, 550, A99

APPENDIX A: YSO ROTATION PERIODS

Table A1. Periodic YSOs identified in this work. We list the *Gaia* DR3 ID number, the RA and Dec. of the source, as well as the period and its uncertainty measured in our data, and the adopted effective temperature. See text for details on the temperature, period, and uncertainty determination.

Gaia DR3 ID	RA	Dec.	Period	Period uncertainty	$T_{\rm eff}$
	(J2000) (°)		(d)	(d)	(K)
1974542739683523584	328.2868	47.11833	2.56542	0.00022	4790
1974545282304297856	328.3771	47.24553	5.81396	0.00031	3911
1974545625901682816	328.4204	47.26174	12.299	0.043	3599
1974545694621155584	328.4209	47.28096	3.42041	0.00064	3848
1974546072578275584	328.3576	47.26427	11.215	0.034	4016
1974546450535495680	328.4107	47.28600	2.88	0.11	4761
1974731890034857600	328.1940	47.21388	3.43143	0.00012	4324
1974731993119999616	328.1718	47.21445	7.7144	0.0016	3721
1974738418391182592	328.2666	47.39185	4.385	0.023	4333
2066866222797779072	312.8774	44.06249	3.165669	0.000034	4681
2066866287224242432	312.8706	44.07308	4.82797	0.00020	6544
2066870689567848192	312.7814	44.17626	3.529858	0.000096	4526
2067058740416252416	312.7431	44.24230	4.87958	0.00029	4654
2067058740416252544	312.7434	44.24562	3.42337	0.00030	4811
2067061042518587264	312.4549	44.17951	3.30949	0.00014	4303
2162929419847388544	313.0956	44.01580	3.63388	0.00057	4722
2162934986124720896	313.3574	44.17924	1.45322	0.00013	4246
2162941273956895872	313.3527	44.34278	2.77937	0.00014	4226
2162944916089431168	313.0939	44.23338	3.00580	0.00027	4259
2162947596149035648	312.8260	44.21893	7.87857	0.00078	4437
2162950413647417728	312.9439	44.37256	2.17499	0.00013	4378
2162950546789495552	313.1453	44.23346	10.63256	0.00027	4373
2162952475231874688	313.1180	44.35405	5.7851	0.0019	4145
2162960481050791936	313.4677	44.28486	7.3719	0.0071	4623
2162964088823157632	313.4243	44.36014	1.4476257	0.0000039	5721
2162965252757133056	313.3618	44.42429	0.626	0.018	5521
2163135573981345280	312.7561	44.25956	5.523	0.048	3929
2163135578281583744	312.7565	44.26166	7.35702	0.00055	4524
2163136059317926016	312.8131	44.30488	4.22803	0.00040	4000
2163136368555566848	312.7190	44.27889	8.312	0.089	4781
2163136402915307136	312.7446	44.29188	7.2271	0.0027	4389
2163137261908777472	312.7776	44.36131	1.3974285	0.0000019	4413
2163137742945115136	312.8445	44.35210	3.882	0.021	4418
2163138601938577024	312.8188	44.38277	2.42438	0.00014	4749
2163139594070911360	312.6920	44.31941	13.69	0.26	3981
2163140319925497088	312.7639	44.40429	5.906	0.011	3842
2163144271295324544	312.9371	44.43861	3.77296	0.00017	4064
2163146779556221952	313.1092	44.57394	1.4325902	0.0000039	4665
2163148772421081728	312.8450	44.56183	4.96431	0.00093	3828
2163156056685634944	312.7258	44.63561	9.5473	0.0031	4011
2178374878170801792	324.5560	57.18633	4.9012	0.0062	4389
2178377901827757056	324.6805	57.30997	10.28020	0.00084	4653
2178383601237749632	324.8094	57.37025	4.03718	0.00041	4267
2178386045086501760	325.0386	57.46087	3.29054	0.00017	4368
2178386938439659392	324.9366	57.51107	0.924	0.035	5538
2178387556914944896	325.0083	57.56533	8.422	0.022	4954
2178391199046443648	324.4901	57.37988	7.57471	0.00039	4597
2178392740924572800	324.4370	57.40375	1.62422	0.00014	4326
2178392848313851392	324.3684	57.39025	16.53	0.36	4589
2178393982185180288	324.3181	57.44453	7.414	0.011	3742
2178394016544915328	324.2946	57.43619	1.3955	0.0039	6417
2178394291422867840	324.4593	57.43017	2.66041	0.00028	4414
2178394394502330496	324.5275	57.45599	1.70361	0.00013	4898
2178394497581292800	324.4461	57.43459	6.0797	0.0018	5218
2178394531941271936	324.4657	57.44790	2.362	0.087	6470
2178394699429915904	324.4628	57.46391	8.5386	0.0015	4066
2178395489703989504	324.4816	57.49225	7.2963	0.0017	4417
2178395631452868224	324.4119	57.49360	10.217	0.039	4137
2178395975050257024	324.4922	57.52218	1.3834638	0.0000030	4495

Table A1 – *continued*

Gaia DR3 ID	RA	Dec.	Period	Period uncertainty	T_{eff}
	(J2000) (°)		(d)	(d)	(K)
2178398895628585984	324.8588	57.52984	2.155	0.036	6198
2178399101787006464	324.8732	57.56156	0.861421747	0.000000069	4876
2178400098219387904	324.8006	57.60453	16.8292	0.0057	4647
2178401575688130688	324.7310	57.59160	8.3030	0.0040	4817
2178402056712608896	324.6082	57.56924	9.30624	0.00048	4507
2178402400321563904	324.5666	57.61572	8.7529	0.0034	4862
2178402606480266112	324.6897	57.63335	3.8835	0.0093	4246
2178402675199735424	324.6682	57.64373	9.9132	0.0011	4442
2178417346809283456	324.0296	57.37860	1.745	0.034	4938
2178421195099930240	324.0530	57.47680	4.645	0.012	5254
2178434938995215232	323.8276	57.56918	11.7067	0.0018	4438
2178440814510995456	324.2248	57.46629	4.16694	0.00050	5558
2178440951949966848	324.2793	57.45021	12.8977	0.0019	4620
2178441261187598208	324.2892	57.49477	3.493	0.021	5008
2178441432986447744	324.2939	57.52010	10.9430	0.0020	4308
2178442188900684032	324.2753	57.53378	1.23416	0.00047	4895
2178443185333123584	324.4591	57.56120	12.924	0.061	4450
2178446793105656704	324.0795	57.63622	7.01448	0.00076	4178
2178449438799259520	324.5703	57.65732	8.0844	0.0019	3699
2178449919842118144	324.6450	57.68859	1.5396700	0.0000031	4755
2178451019353727104	324.5940	57.73136	6.4447	0.0018	5109
2178452668621309568	324.6846	57.79075	9.66039	0.00097	4829
2178498882466387072	324.9171	57.78227	5.6398	0.0012	4646
2221015863228441856	325.6784	66.20783	0.63188429	0.00000050	5570
3016871585188001536	84.1696	−6.86793	0.60243683	0.00000015	3826
3016879556647282816	84.4641	−6.66429	0.80573197	0.00000044	5067
3016882374145831680	84.4283	−6.67111	3.74654	0.00097	5085
3016904192579682176	84.6331	−6.60688	1.422	0.060	3697
3016935563020738688	84.2457	−6.48469	10.698	0.020	3618
3016957278375450752	84.5426	−6.42406	3.37636	0.00060	3970
3017197830905390592	83.8739	−5.81251	1.7518139	0.0000088	4859
3017199170935143680	84.1010	−5.74686	5.9794	0.0065	4475
3017237993141611776	83.6677	−5.83767	2.3913	0.0082	5639
3017244216552060672	83.6985	−5.73077	4.2183	0.0059	5324
3017245831459893760	83.7997	−5.76055	4.0381	0.0018	4354
3017246651795678720	83.8245	−5.70969	5.52737	0.00075	5298
3017250087773385344	83.8042	−5.65970	3.048676	0.000059	5886
3017250126427057024	83.7124	−5.70597	3.1840	0.0065	5261
3017251947493281536	83.9301	−5.60763	2.6630	0.0025	5522
3017265377852811776	83.8067	−5.51602	8.505	0.013	5316
3017265760107995904	83.7353	−5.52672	5.740282	0.000063	5227
3017266168126793984	83.7625	−5.50042	5.0828	0.0044	5059
3017266206784582144	83.7877	−5.49979	4.07794	0.00047	5258
3017267306296233216	83.6465	−5.53622	5.12	0.14	5438
3017267478094926720	83.6154	−5.53204	3.37257	0.00040	5957
3017270669252519680	83.6883	−5.41780	3.45359	0.00024	5576
3017291942240221056	84.2538	−5.69361	3.1916	0.0073	5109
3017346952181228416	83.8743	−5.54819	3.9141	0.0034	5795
3017347291470793216	83.8849	−5.51979	2.313	0.033	6301
3017355400367313024	84.1339	−5.39586	4.020	0.011	6516
3017359527845298048	83.8955	−5.48734	2.532	0.075	4294
3017364544367271936	83.7113	−5.40034	2.35	0.11	5190
3017364613086735360	83.7332	−5.38696	17.35	0.34	6176
3017367494996951424	83.8269	−5.27713	3.76	0.17	4345
3017368014699258240	84.0437	−5.32917	6.03019	0.00042	4796
3017371588112037248	84.0708	−5.19522	7.38	0.32	5038
3017373924574255488	83.9282	−5.19855	3.29813	0.00053	4819
3017374233811898880	83.9422	−5.18107	3.59665	0.00014	3976
3017375951801904256	83.9652	−5.13590	2.82524	0.00065	5424
3017382407121669504	84.2156	−5.22499	2.48995	0.00053	5193

Table A1 – *continued*

Gaia DR3 ID	RA (J2000) (°)	Dec.	Period (d)	Period uncertainty (d)	$T_{\rm eff}$ (K)
3046357806990068096	107.0442	−10.76915	1.1351	0.0022	5861
3046581110929906560	107.1821	−10.41369	2.3871	0.0061	5140
3209521037582290304	83.7599	−5.26332	6.0803	0.0017	5226
3209522618130302720	83.7368	−5.19250	3.97728	0.00059	5020
3209527634652049408	83.8477	−5.18104	7.65863	0.00045	3928
3209528012609165440	83.9128	−5.14900	6.7452	0.0052	5199
3209528523708699392	83.8055	−5.15549	9.742	0.052	4412
3209528905962364544	83.8595	−5.14445	2.7453	0.0028	5946
3216061001461614976	84.7167	−2.77882	10.763	0.083	4510
3216062272771926144	84.7216	−2.73141	7.8142	0.0059	3931
3216107490187638784	84.6136	−2.75270	7.0805	0.0026	4332
3216109861009561728	84.6843	−2.67216	10.890	0.011	4623
3216432464593272960	84.8872	−2.79701	2.70295	0.00042	4460
3216439023007610624	84.8857	−2.66224	6.8943	0.0019	5105
3216439847641330816	84.8550	−2.63946	9.762	0.022	4405
3216446547790307584	84.9493	−2.54026	1.57340	0.00015	4934
3216446689524900480	84.9687	−2.53400	12.923	0.039	4736
3216447239280699008	85.0141	−2.48375	7.357	0.031	4505
3216485722187722752	84.7985	−2.60080	12.1119	0.0058	4488
3216487749412405376	84.8453	−2.55920	7.2427	0.0017	3760
3216488329232163328	84.7725	−2.54177	5.7223	0.0047	4678
3216490223313304576	84.6478	−2.53103	10.4049	0.0044	4824
3216491151026233472	84.6678	−2.50516	7.8721	0.0011	4208
3216492869013787264	84.7002	−2.45393	8.4758	0.0082	4875
3216502798977562112	84.5281	−2.50632	7.3507	0.0020	3875

[1]*Centre for Astrophysics and Planetary Science, School of Engineering, Mathematics and Physics, University of Kent, Canterbury CT2 7NH, UK*
[2]*Royal Museums Greenwich, Romney Road, London SE10 9NF, UK*
[3]*SUPA, School of Physics & Astronomy, University of St Andrews, North Haugh, St Andrews KY16 9SS, UK*
[4]*Public observatory ASTROLAB IRIS, Provinciaal Domein 'De Palingbeek', Verbrandemolenstraat 5, B-8902 Zillebeke, Ieper, Belgium*
[5]*Vereniging Voor Sterrenkunde (VVS), Zeeweg 96, B-8200 Brugge, Belgium*
[6]*Centre for Mathematical Plasma-Astrophysics, Department of Mathematics, KU Leuven, Celestijnenlaan 200B, B-3001 Heverlee, Belgium*
[7]*Thüringer Landessternwarte, Sternwarte 5, D-07778 Tautenburg, Germany*
[8]*American Association of Variable Star Observers (AAVSO), 185 Alewife Brook Parkway, Suite 410, Cambridge, MA 02138, USA*
[9]*Variable Stars South (VSS), Royal Astronomical Society of New Zealand, PO Box 3181, Wellington, New Zealand*
[10]*MCD Observatory, 23 Langlois, Saint-Anaclet, QC G0K 1H0, Canada*
[11]*Variable Star Section, British Astronomical Association, PO Box 702, Tonbridge TN9 9TX, UK*
[12]*Bath Astronomers, 19 New King Street, Bath BA1 2BL, UK*
[13]*Flamsteed Astronomy Society, Royal Observatory Greenwich, Blackheath Avenue, London SE10 8XJ, UK*
[14]*Observadores de Supernovas (ObSN), Spain, https://www.obsn.es/*
[15]*Science Department, Seville University, Av de la Ciudad Jardín 20-22, E-41005 Sevilla, Spain*
[16]*Dark Skies New Mexico Observatory, 1984 W Golden Rose Pl, Oro Valley, AZ 85737, USA*
[17]*R.P. Feynman Observatory, Piazzetta del Gesú 3, I-73034 Gagliano del Capo, Italy*
[18]*Center for Backyard Astrophysics (CBA), Piazzetta del Gesú 3, I-73034 Gagliano del Capo, Italy*
[19]*Hampshire Astronomical Group, Hinton Manor Lane, Clanfield PO8 0QR, UK*
[20]*Royal Astronomical Society, Burlington House, Piccadilly, London W1J 0BQ, UK*
[21]*Bundesdeutsche Arbeitsgemeinschaft für Veränderliche Sterne (BAV), Munsterdamm 90, D-12169 Berlin, Germany*
[22]*Sternwarte Neanderhoehe Hochdahl, Sedentaler Str 105, D-40699 Erkrath, Germany*
[23]*Observatorio de Sencelles, Sonfred Road 1, E-07140 Sencelles, Mallorca, Spain*
[24]*Dimension Point Observatory, 14 Galaxy Point, Mayhill, NM 88339, USA*
[25]*Green Island Observatory, Karaoğlaonoğlu Street 63A, 99610 Geçitkale, Mağusa, North Cyprus*
[26]*Crayford Manor House Astronomical Society, Parsonage Lane Pavilion, Parsonage Lane, Sutton-at-Hone, Dartford DA4 9HD, Kent, UK*
[27]*Groupe Européen d'Observations Stellaires (GEOS), 23 Parc de Levesville, F-28300 Bailleau l'Evêque, France*
[28]*Cerro del Viento Observatory (MPC I84), Fernandez Pirfano Square 3, E-06010 Badajoz, Spain*
[29]*Sociedad Malagueña de Astronomía (SMA), Centro Cultural José María Gutiérrez Romero, Cl República Argentina, no 9, Urb. El Limonar, E-29016 Málaga, Spain*
[30]*Cal Maciarol módul 8 Observatory, Masia Cal Maciarol, Camí de l'Observatori S/N, E-25691 Àger, Spain*
[31]*Department of Electronics, Electrical Engineering and Microelectronics, Silesian University of Technology, Akademicka 16, PL-44-100 Gliwice, Poland*
[32]*Horndean Observatory, 6 Falcon Road, Horndean, Waterlooville, Hampshire PO8 9BY, UK*
[33]*The Herschel Society, The Herschel Museum of Astronomy, 19 New King Street, Bath BA1 2BL, UK*
[34]*Center for Backyard Astrophysics Extremadura, E-06340 Fregenal de la Sierra, Spain*
[35]*Vereniging voor Sterrenkunde VVS, B-3401 Landen, Belgium*
[36]*Selztal Observatory, Bechtolsheimer Weg 26, D-55278 Friesenheim, Germany*
[37]*The Studios Observatory (MPC Z52), 31 Ipswich Gardens, Grantham NG31 8SE, UK*
[38]*Osservatorio Conigliolo, Via Chiantigiana, I-50055 Ginestra Fiorentina, Firenze, Italy*

[39] *Saptarishi India, 1/125-G New Civil Lines, Navadiya, Fatehgarh, Farrukhabad 209601, Uttar Pradesh, India*
[40] *Akash Ganga: Centre for Astronomy, A/2 East & West Villa, Nowroji Vakil Street, Grant Road, Mumbai 400007, Maharashtra, India*
[41] *La Vara, Valdes Observatory(MPC J38), Barrio La Bara, sin número Muñas de Arriba código postal, E-33784 Asturias, Spain*
[42] *Asociacion Astronomica Cruz del Norte, Calle Caceres 18, E-28100 Alcobendas, Madrid, Spain*
[43] *Astronomical Institute, University of Wrocław, ul. M. Kopernika 11, PL-51-622 Wrocław, Poland*
[44] *Astronomical Observatory, University of Warsaw, Al. Ujazdowskie 4, PL-00-478 Warsaw, Poland*
[45] *Astrophysics Division, National Centre for Nuclear Research, Pasteura 7, PL-02-093 Warsaw, Poland*

This paper has been typeset from a TEX/LATEX file prepared by the author.